RESEARCH ARTICLE | OCTOBER 01 2024

The formation and post-formation processes of vortex rings discharged from laminar starting jets ⊘

Haojun Zheng (郑浩均) ⓘ ; Lei Gao (高磊) ✉ ⓘ ; Simon C. M. Yu (余澄文) ⓘ

Check for updates

View Online   Export Citation

Articles You May Be Interested In

Interaction between a laminar starting immersed micro-jet and a parallel wall

Physics of Fluids (January 2015)

Effect of slip on existence, uniqueness, and behavior of similarity solutions for steady incompressible laminar flow in porous tubes and channels

Physics of Fluids (August 2006)

Lagrangian analysis of the laminar flat plate boundary layer

Physics of Fluids (October 2016)

Physics of Fluids

The formation and post-formation processes of vortex rings discharged from laminar starting jets

Haojun Zheng (郑浩均),[1] [iD] Lei Gao (高磊),[2,a] [iD] and Simon C. M. Yu (余澄文)[1] [iD]

AFFILIATIONS

[1]Department of Aeronautical and Aviation Engineering, The Hong Kong Polytechnic University, Kowloon, Hong Kong,
People's Republic of China
[2]School of Aeronautics and Astronautics, Sichuan University, Chengdu 610065, People's Republic of China

[a]Author to whom correspondence should be addressed: lei.gao@scu.edu.cn

ABSTRACT

Motivated by biological systems, vortex rings can enhance the propulsive efficiency in industrial systems. To study the vortex properties during the formation and post-formation stages, impulsively starting jets are investigated by simulations. The effects of the stroke ratio and nozzle geometry are studied at a fixed jet Reynolds number of 2500. The stroke ratio at the formation number is found to be not enough to produce a vortex ring with maximum circulation. The stroke ratio is suggested to be about twice as large as the formation number. An alternative criterion based on the circulation ratio is proposed to describe the onset of pinch-off. This criterion states that the pinch-off would start when the vortex ring attains about 80% of the total jet circulation. During the formation stage, the scaling laws for vortex trajectories and circulation are proposed for continuous formation. By combining the suggested scaling relations and Saffman's velocity formula, the evolution of non-dimensional energy can be predicted. During the post-formation stage, the scaling laws for vortex properties (e.g., the vortex ring diameter, translational velocity, and circulation) are found to be independent of both the nozzle configuration and the vortex Reynolds number. On the grounds of the invariance of impulse in vortex decay, the scaling laws of vortex motion are derived for the non-dimensional energy, circulation, and diffusivity scale of the vortex core. In consequence, the normalized energy and circulation found in experiments can be successfully derived from the similarity model for both nozzle configurations.

NOMENCLATURE

a	Radius of the vortex ring core
a_I	Scaling factor of I_v^*
a_R	Scaling factor of R_v^*
a_U	Scaling factor of U_v^*
a_{ne}	Constant used to fit the evolution of vortex energy
a_r	Scaling factor of r_v^*
a_x	Scaling factor of x_v^*
a_Γ	Scaling factor of Γ_v^*
a^*	Dimensionless radius of the vortex core $a^* = a/D$
b_{ne}	Constant used to fit the evolution of vortex energy
D	Diameter at the nozzle exit
D_p	Diameter of the piston
D_v	Diameter of the vortex ring
D_v^*	Dimensionless vortex diameter $D_v^* = D_v/D$
E	Kinetic energy
E_t	Total energy
E_v	Vortex energy
$E_{v\max}$	Local maximum of the vortex energy
E_v^*	Dimensionless vortex energy $E_v^* = E_v/\rho U_{max}^2 D^3$
E_v^{**}	Dimensionless vortex energy $E_v^{**} = E_v/(\rho I_v \Gamma_v^3)^{1/2}$
F	Formation number
I	Hydrodynamic impulse
I_t	Total impulse
I_v	Vortex impulse
$I_{v\max}$	Local maximum of the vortex impulse
I^*	Dimensionless vortex impulse $I_v^* = I_v/\rho U_{max} D^3$
L	Stroke length over the nozzle exit
L_m	Maximum stroke length
L/D	Stroke ratio
L_m/D	Maximum stroke ratio

R_v	Radius of the vortex ring
Re_D	Jet Reynolds number $Re_D = U_{max}D/\nu$
Re_{UD}	Vortex Reynolds number $Re_{UD} = (U_vD_v)_{max}/\nu$
Re_Γ	Vortex Reynolds number $Re_\Gamma = \Gamma_{vmax}/\nu$
R_v^*	Dimensionless vortex radius $R_v^* = R_v/D$
r_v	Vortex radial trajectory from the nozzle exit edge
r_v^*	Dimensionless radial trajectory $r_v^* = r_v/D$
t	Physical time
t_0	Virtual origin time
t_1	Acceleration and deceleration duration of the piston motion
t_2	Shift time
t_p	Jet discharge time defined by $L_m/D = U_{max}t_p$
t^*	Dimensionless formation time $t^* = \overline{U}_0t/D$
t^{**}	Dimensionless time $t^* = \overline{U}_{max}t/D$
U_0	Space-averaged velocity over the nozzle exit
U_{max}	Time-maximum velocity at the nozzle exit
U_p	Piston velocity
U_v	Vortex translational velocity
U_v^*	Dimensionless vortex velocity $U_v^* = U_v/U_{max}$
$\overline{U}_0$	Time-averaged velocity at the nozzle exit
x, r, θ	Coordinates of a three-dimensional cylindrical coordinate system
x_v	Vortex axial trajectory from the nozzle exit center
x_v^*	Dimensionless axial trajectory $x_v^* = x_v/D$
Γ	Circulation
Γ_t	Total circulation
Γ_{tmax}	Local maximum of the total circulation
Γ_v	Vortex circulation
Γ_{vmax}	Local maximum of the vortex circulation
Γ^*	Dimensionless circulation $\Gamma^* = \Gamma/U_{max}D$
Γ_v^{**}	Dimensionless vortex circulation $\Gamma_v^{**} = \Gamma_v/(\rho^{-1}I_vU_v^2)^{1/3}$
Δr	Grid spacing in r direction
Δx	Grid spacing in x direction
$\overline{\Delta r}$	Averaged grid spacing in r direction
ε	Mean core radius of the vortex ring $\varepsilon = a/R_v$
μ	Dynamic viscosity
ν	Kinematic viscosity
ρ	Fluid density
Ψ	Stokes stream function
ω	Azimuthal vorticity

I. INTRODUCTION

Vortex rings can be widely observed in biological systems, such as aquatic locomotion and blood flow in the cardiac left ventricle.[1] Moreover, vortex ring formation is also a fundamental issue in natural systems, such as the spread of dandelion seeds[2] and volcanic eruption.[3] In ocean engineering, vortex rings can be used to enhance propulsive efficiency[4,5] due to the added mass transport in the vortex ring formation.[6] These scenarios catch the attention of research community on the kinematics and dynamics of vortex rings.

In the laboratory, an axisymmetric vortex ring is usually generated by a piston pushing a column of fluid through a tube or orifice nozzle into a quiescent environment. Laminar vortex rings generally go through the formation (before a completed pinch-off) and post-formation (after completed formation and stabilization) stages in their development.[7] During the formation stage, the scaling laws for vortex

trajectory have been discussed in tube-based experiments,[8] which were found to be insensitive to Re for sufficiently high Reynolds numbers in the laminar regime. The self-similarity of vortex roll-up could be partially predicted by theoretical models,[9,10] such as the radial trajectory obeying a time-dependent form $\sim t^{2/3}$. However, due to the effects of the self-induced velocity of the vortex ring and the downstream component of the starting flow, the form suggested by theoretical models $\sim t^{2/3}$ is not successful in predicting the experimental axial trajectory, which was found to be in the form of $\sim t^{3/2}$. This contradiction found in experiments was also confirmed by simulations.[11,12] Most previous laminar studies focused on the small stroke ratio ($L_m/D \leq 1.6$) and the kinematic properties of tube-generated vortex rings. Orifice cases and large-stroke-ratio cases need more investigations. During the post-formation stage, the scaling laws for the decay of translational velocity and the growth of vortex ring diameter were proposed by orifice-based experiments[13] and simulations for parallel jets.[14] The effects of the vortex Reynolds number on the scaling relations for either tube-generated or orifice-generated vortex rings remain undetermined.

The dynamical properties of vortex rings were found crucial in their formation process, such as the vortex circulation, hydrodynamic impulse, and kinetic energy.[15] A critical stroke ratio (i.e., the formation number) was found to be at about 4, corresponding to a maximum vortex ring formation with the absence of a trailing jet.[16] The energy and circulation in a non-dimensional form for an optimal vortex ring were universal at about 0.3 and 2, respectively.[17] Further simulations verified these invariances in parallel jets.[14,18] In addition, these invariances were extended to the non-parallel starting jet generated by an orifice nozzle.[19]

The dynamical properties of vortex rings were usually identified only when vortex rings were far away from the trailing jet. With the development of Lagrangian analysis, the rear boundary of the vortex ring can be identified even without a clear separation of the vorticity field from the trailing jet.[20] On the other hand, a trailing pressure maximum was locally observed and regarded as the rear boundary of the vortex.[20] This high-pressure region creates a barrier repelling the fluid from the trailing jet.[21] The pressure-based vortex boundary was recently found to be comparable with the Lagrangian vortex boundaries, leading to a reduction in the computational time.[22] The pressure-based method would therefore be beneficial to further investigations for the temporal evolutions during the vortex ring formation.

Based on the idea of vorticity shedding from a nozzle during the formation stage, the dynamical properties (i.e., the invariants of motion) of vortex rings were predicted by a family of slug models, including the classical one[8] and the revised ones.[23,24] For the self-similarity of axisymmetric vortex rings, the temporal evolution of kinematic properties (i.e., the axial and radial trajectories) could be well predicted by theoretical and experimental results. However, the kinematic properties have not yet been used in analyzing the dynamical properties, such as the non-dimensional circulation and energy.

To this end, the main objective of our study is to examine the formation and post-formation processes of vortex rings discharged from laminar starting jets. More details on the limiting vortex formation are discussed. The stroke ratios are available over a wide range, and the nozzle configurations include both tube and orifice nozzles. Scaling laws for trajectories are studied for an extensive formation time. Through a bridge between the kinematic properties and the dynamical properties, the non-dimensional energy and circulation are expected to

be predicted appropriately for the formation and post-formation stages.

The paper is organized as follows. The numerical setup, verification, and validation are introduced in Sec. II. A brief introduction to the kinematics and dynamics of vortex rings is introduced in Sec. III. In Sec. IV, the growth of vortex invariants is studied for a better understanding of the dynamics of vortex formation. A similarity model during the vortex formation stage is proposed to predict the kinematic and dynamical properties. Based on the proposed similarity relations, the evolution of the non-dimensional energy is suggested. The scaling laws for the non-dimensional energy, circulation, and core radius during vortex post-formation are derived from Maxworthy's model and Saffman's velocity formula. Finally, concluding remarks are provided in Sec. V.

II. NUMERICAL METHOD

A. Problem statement

The computational domains are presented in Figs. 1(a) and 1(b). A fluid column of the stroke length $L(t)$ is pushed through a nozzle with a diameter D. The origin of coordinates is located at the center of the nozzle exit, and the nozzle axis is aligned with the x direction. The distance between the nozzle inlet and nozzle exit is fixed at $40D$. The outer boundary is placed at a lateral distance of $3D$ from the axis. The downstream boundary is placed at a streamwise distance of $40D$ from the nozzle exit. A squared-off lip at the orifice is used to avoid the singularity.

The no-slip condition is enforced on the nozzle wall and the outer orifice plate. The pressure outlet with zero gauge pressure is employed on the outer and downstream exits. The piston is modeled as a time-dependent velocity inlet boundary.[25–27] A uniform velocity profile is specified at the nozzle inlet to control piston velocity $U_p(t)$. To avoid singularity, acceleration and deceleration phases with duration t_1 are considered and are short to model the impulsive motion of the piston. To make the effects of acceleration and deceleration phases negligible, these phases should be as short as possible, such as $t_1^{**} = U_{max}t/D = 0.1$, where U_{max} is the maximum velocity at the nozzle exit. As proposed in

TABLE I. Key parameters in cases.

Case	Geometry	$\overline{U}_0$ (cm/s)	L_m/D
T1	Tube	11.72	1.5
T2	Tube	12.10	3
T3	Tube	12.30	6
T4	Tube	12.36	9
T5	Tube	12.42	15
O1	Orifice	11.36	1
O2	Orifice	11.72	1.5
O3	Orifice	11.90	2
O4	Orifice	12.10	3
O5	Orifice	12.20	4

the previous simulations,[28] the velocity program at the nozzle exit is defined as

$$U_0(t) = \begin{cases} 0.5U_{max}\left[1 - \cos\left(\dfrac{t}{t_1}\pi\right)\right] & \text{for} \quad t \le t_1, \\ U_{max} & \text{for} \quad t_1 < t \le t_p, \\ 0.5U_{max}\left[1 + \cos\left(\dfrac{t - t_p}{t_1}\pi\right)\right] & \text{for} \quad t_p < t \le t_p + t_1, \\ 0 & \text{for} \quad t > t_p + t_1. \end{cases} \quad (1)$$

Based on the nozzle exit velocity $U_0(t)$ and the end of the constant velocity t_p determined by $L_m/D = U_{max}t_p$, the time-averaged velocity and maximum stroke length are expressed as $\overline{U}_0 = (t_p + t_1)^{-1}\int_0^{t_p+t_1} U_0 dt$ and $L_m = \int_0^{t_p+t_1} U_0 dt$. The non-dimensional time is defined as $t^* = \overline{U}_0 t/D$.

A total of 10 cases are simulated, as shown in Table I. Water is used as the working fluid, with density $\rho = 998.2 \text{ kg/m}^3$ and dynamic viscosity $\mu = 1.003 \times 10^{-3} \text{ kg/ms}$. The same exit diameter $D = 2 \text{ cm}$ and maximum exit velocity $U_{max} = 12.5 \text{ cm/s}$ for both tube and
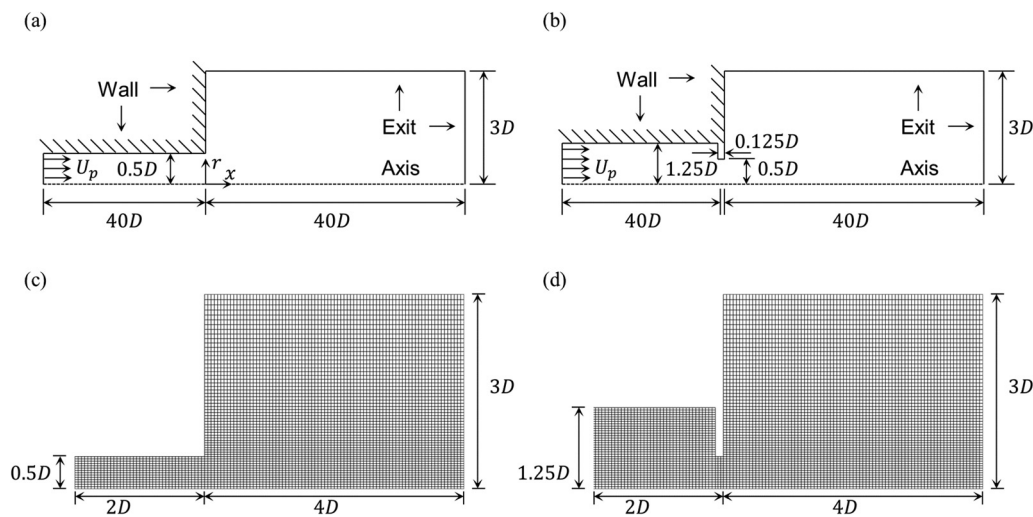

FIG. 1. Computational domains (not to scale) for (a) tube and (b) orifice. Sample meshes (every sixth mesh point is shown in each direction) for (c) tube and (d) orifice.

TABLE II. Mesh for grid independent tests.

Nozzle	$\Delta x = \overline{\Delta r}$	Mesh outside nozzle	Total cell number
Tube	$D/50$	2001×151	3.7×10^5
Tube	$D/100$	4001×301	1.5×10^6
Tube	$D/150$	6001×451	3.3×10^6
Orifice	$D/50$	2001×151	4.8×10^5
Orifice	$D/100$	4001×301	1.9×10^6
Orifice	$D/150$	6001×451	4.3×10^6

orifice provide a fixed jet Reynolds number $\mathrm{Re}_D = U_{\max}D/\nu = 2500$, where ν is the kinematic viscosity.

B. Mathematical formulation and numerical method

The axisymmetric, unsteady, incompressible, and laminar Navier–Stokes equations are solved by the commercial finite volume package ANSYS Fluent. The pressure-implicit with splitting of operators (PISO) algorithm with the non-iterative time advancement scheme is used for pressure velocity coupling. Second-order schemes are used in spatial and temporal discretization. The computational domains are discretized by structured meshes. The grid is uniform in the axial direction with a spacing $\Delta x = D/100$ and is non-uniform in

the radial direction with a higher density near the axis. The average spacing in the radial direction is $\overline{\Delta r} = D/100$. The high-resolution simulations are employed with 4001×301 grid points outside the nozzle. Sample meshes for the tube and orifice cases are partially shown in Figs. 1(c) and 1(d) (for clarity only every sixth mesh point is shown in each direction). The time step is fixed at 0.001 s, which ensures that the cell Courant numbers are less than one for all cases.

C. Verification and validation

The influence of the computational domain size on flows is tested for vortex ring radius. In comparison with larger domains $40D \times 5D$, the errors of ring radius (i.e., the radial position of the vorticity peak fitted by the Gaussian distribution) are less than 3% for both nozzles. To evaluate the grid sensitivity, cases with fewer and more grids as shown in Table II are tested. In comparison with the denser meshes, the present meshes perform well for both nozzles [Fig. 2(a)]. For case T5, the error is smaller than 1%. For case O5, the error is less than 3%. In the time step tests, the errors are less than 2% for both nozzles in comparison with the time step 0.0005 s [Fig. 2(b)]. To summarize, the present grid distributions and the time step are sufficient to describe the flow adequately.

Following the same Reynolds number of numerical study,[25] tube case T3 [Fig. 3(a)] is well validated with the experimental case with a stroke ratio of 6[16] for both total circulation and vortex circulation.
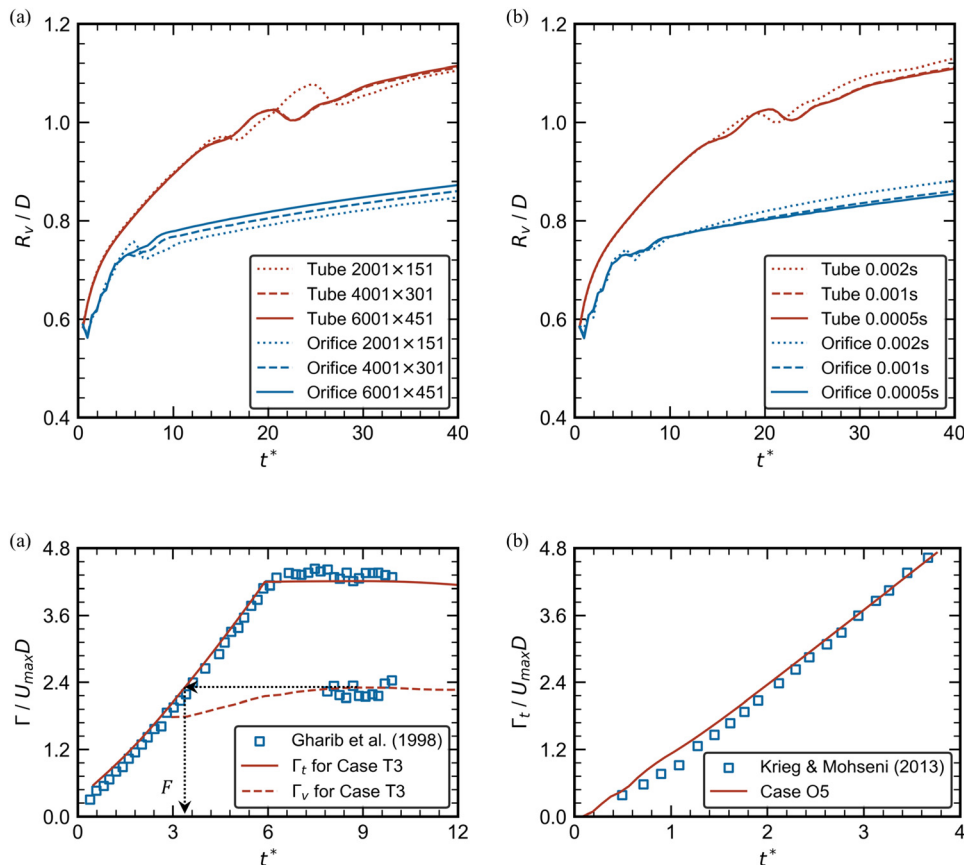
FIG. 2. Independent tests on ring radius for (a) grid sizes and (b) time steps.

FIG. 3. Validations with experiments by (a) total circulation as well as vortex circulation for tube nozzle and (b) total circulation for orifice nozzle.

The formation number ($F = 3.4$) identified from case T3 basically agrees well with the one (3.6) found in the experiment. Orifice case O5 [Fig. 3(b)] is modified by increasing the acceleration phase to t_1^{**} = 0.4 to validate the experimental case with a stroke ratio of 6.8.[23] Our result agrees well with the experiment within the maximum stroke ratio in our study.

III. KINEMATICS AND DYNAMICS OF VORTEX RINGS

As shown in Fig. 4, the vortex bubble includes the rotational fluid (elliptical vortex core) and irrotational fluid. The core center is determined by the local maximum vorticity correlated by the Gaussian distribution. The ring diameter D_v is the distance between the upper center and the lower center. The ring radius is defined as R_v. Based on Saffman,[9] the axial and radial trajectories (x_v and r_v) are the horizontal and vertical distances from the core center to the nozzle edge. From the first-order derivative of axial trajectory with respect to time, the ring translational velocity U_v is obtained by the fourth-order central-difference approximation. In the theory of vortex ring, the vortex core is usually assumed to be a circular geometry.[9] The core radius a is determined by the equivalent vortex core where the area is equivalent to the real elliptical core. With the mean core radius $\varepsilon = a/R_v$,[29] the core radius can be obtained from the non-dimensional vortex energy by a fitting procedure to a vortex family.[14,30]

The dynamical properties are the invariants of vortex motion, namely, the circulation Γ_v, impulse I_v, and energy E_v. They are determined by the area integration within the vortex bubble, i.e.,

$$\Gamma_v = \iint \omega \, dr \, dx, \quad I_v = \rho\pi \iint \omega r^2 \, dr \, dx, \quad \text{and} \quad E_v = \rho\pi \iint \omega \Psi \, dr \, dx, \quad (2)$$

where ω is the azimuthal vorticity and Ψ is the Stokes stream function. The non-dimensional energy and circulation, identifying the geometric parameter ε of vortex rings,[29,31] are defined as

$$E_v^{**} = \frac{E_v}{(\rho I_v \Gamma_v^3)^{1/2}} \quad \text{and} \quad \Gamma_v^{**} = \frac{\Gamma_v}{(\rho^{-1} I_v U_v^2)^{1/3}}. \quad (3)$$

To obtain the vortex boundary for calculating the above-mentioned integrations, the cutoff level is 5% of the local maximum vorticity.[25,28] This cutoff level in the vorticity field is sufficient to include the inner core of the leading vortex.[14] Sensitivity analysis had been made by the cutoff level of 2%. The differences in the vortex invariants are within 5% for both nozzle configurations. Therefore, the vortex invariants are found to be insensitive to the choice of the cutoff
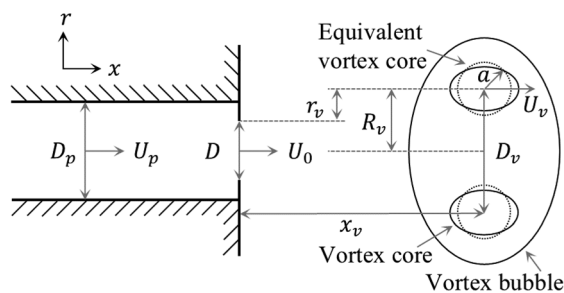

FIG. 4. Key kinematic parameters of vortex rings.

level. With the use of the pressure-based method to identify the vortex rear boundary,[22] the vorticity upstream of the trailing pressure maximum on the centerline is excluded in the calculation of vortex invariants. In Fig. 5, rows from top to bottom are the absolute pressure value along the axis, streamlines in the reference frame moving with the vortex ring, and vorticity contours, respectively. A trailing pressure maximum is developed on the symmetry axis [Figs. 5(a) and 5(d)], corresponding to the rear stagnation point of the vortex bubble [Fig. 5(e)]. At early times [Fig. 5(c)], some vorticity of the trailing jet is being absorbed inside the vortex bubble. A clear separation between the vortex ring and the trailing jet can only be identified later [Fig. 5(f)].

IV. RESULTS AND DISCUSSION
A. Vortex formation for both tube-generated and orifice-generated starting jets

The upper limit of vortex circulation growth has been experimentally confirmed in tube-generated[16] and orifice-generated[19] starting jets. The critical timescale in a non-dimensional form was referred to as the formation number F, which was determined when the total circulation became equal to the locally maximum vortex circulation.[25]

The limiting development of vortex dynamical properties would be further studied in this section. First of all, the appearance of pinch-off is confirmed by the vorticity field. As shown in Fig. 6, the maximum stroke ratios considered in the present study are large enough to identify the formation number (i.e., the critical stroke ratio for the state transition of the starting jet) for the tube and orifice cases because the pinch-off between the leading vortex ring and the trailing jet can be clearly observed after the jet discharge. During the initial time ($t^* \leq 1$), the vortex ring grows by absorbing the positive vorticity shedding from the nozzle edge. The negative vorticity produced can also be observed for the tube and orifice cases, while it is stronger for the orifice cases due to the larger vortex strength from the over-pressure effect. Therefore, the orifice-generated vortex would become slightly unstable due to the effects of converging flow and negative vorticity. At the moment of the final stroke ratio for each nozzle [Figs. 6(d) and 6(i)], the orifice-generated vortex ring clearly separates from the tailing jet, while the tube-generated vortex ring still connects with the trailing jet in the vorticity field.

Following the circulation method and excluding the vortex pairing situation,[16] the formation numbers are found to be 4.6 (from case T5) and 2.2 (from case O5) for the tube and orifice, respectively, when the total circulation reaches the maximum vortex circulation (Fig. 7). These results are in good agreement with experiments.[16,19] It is noted that the leading vortex ring of case T5 can reach the limiting state of circulation before the vortex pairing. For the orifice case O5, the leading vortex ring nearly reaches the limiting vortex circulation due to the convergence of the maximum vortex circulation with respect to the stroke ratio (further discussed below).

To study the dynamical properties quantitatively, the evolution of vortex circulation $\Gamma_v^* = \Gamma_v/U_{max}D$, impulse $I_v^* = I_v/\rho U_{max}D^3$, and energy $E_v^* = E_v/\rho U_{max}^2 D^3$ are presented in Fig. 8. The first and second rows are for the tube and orifice, respectively. Generally, the vortex invariants (Γ_{vmax}^*, I_{vmax}^*, and E_{vmax}^*) representing the local maximum increase with the stroke ratio L_m/D. This result is not fully in agreement with the prior conclusion that the maximum vortex circulation was found to be independent of the final stroke ratio when it was
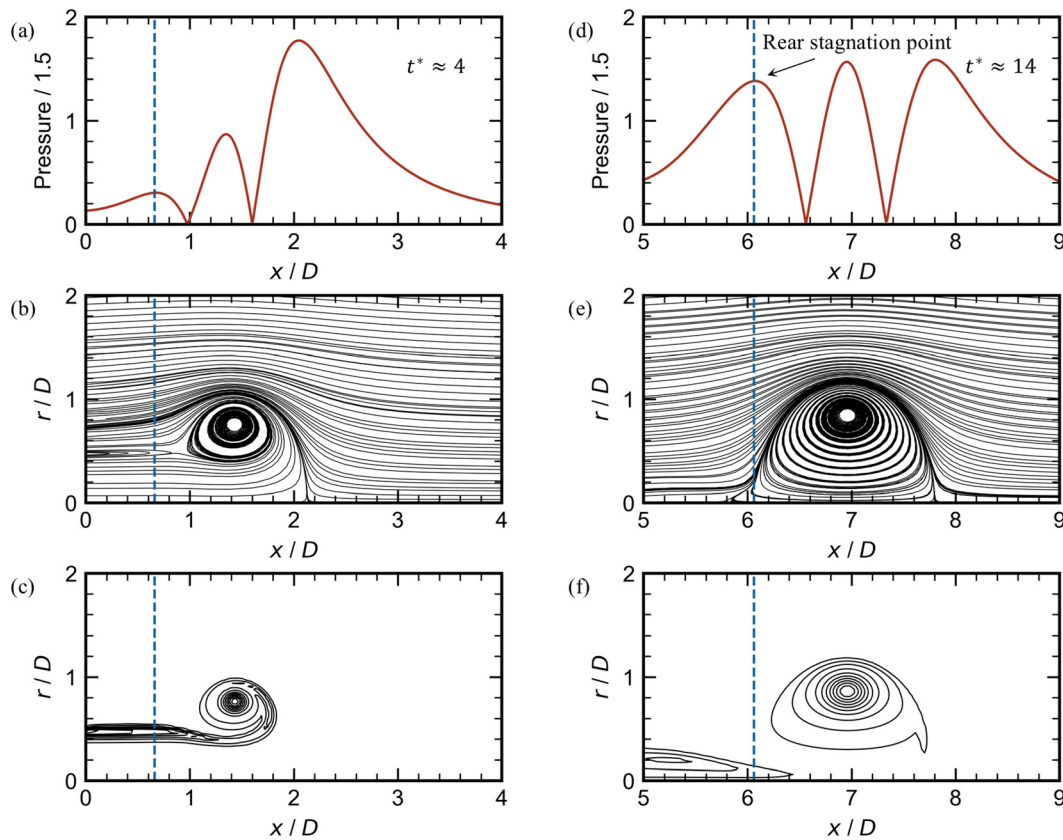
FIG. 5. Pressure-based vortex boundary (case T3). Rows represent (a) and (d) the absolute pressure along the axis in SI unit, (b) and (e) the streamlines in the reference frame moving with the vortex ring, and (c) and (f) the vorticity contours normalized by local maximum (from 0.05 to 1, with 11 levels).

slightly larger than the formation number.[16] This corresponds to the later instant when the complete pinch-off can be observed in simulations such as the case T3 shown in Fig. 5(f) and other numerical studies.[14,25] In comparison with case T3, the vortex circulation of case T4 increases by 27%. There is a corresponding increase of 27% in the formation number (from 3.4 to 4.3). The limiting circulation could be observed in case T5 before the increase by the vortex pairing at $t^* = 18$ [Fig. 8(a)]. This situation is similar to the previous simulation,[32] but the vortex pairing occurs earlier due to a larger Reynolds number in the present study. It is noted that the vortex pairing situations (after the appearance of Kelvin–Helmholtz instability in the trailing jet) found in experiments[16,33] are both at around $t^* = 11$ for smaller Reynolds numbers. Excluding the vortex pairing, the vortex circulation for case T5 increases by 6%. There is a corresponding increase of 6% in the formation number in comparison with case T4. These results suggest that the case of stroke ratio 6 cannot generate the maximum vortex ring circulation, but the case of stroke ratio 9 ($L_m/D \approx 2F$) can nearly achieve it. For the orifice cases, in comparison with case O4, the vortex circulation of case O5 ($L_m/D \approx 2F$) increases by 2%. There is a corresponding increase of 2% in the formation number [Fig. 6(b)]. These results suggest that a stroke ratio larger than the formation number would be necessary to produce a vortex ring achieving the state of maximum invariants. The tube case with stroke ratio 12 ($L_m/D \approx 3F$)

presents a similar vortex pairing phenomenon (not shown here). Thus, the stroke ratio is suggested to be twice the formation number in order to produce a vortex ring at the state of maximum invariants. This suggestion agrees well with the experimental measurements for the orifice case.[19]

It is noted that the continuous increase in impulse and energy after the piston motion stopped[19] only appears in case T5 [Figs. 8(c) and 8(e)]. It can be attributed to the effect of the vortex pairing. During the pairing process, the vortex core becomes slightly distorted and axially elongated, leading to a temporal increase in the core area. The increase in impulse and energy disappears later at the post-formation stage.

To study the capability to transform jet flow into vortex motion, the ratio of the maximum vortex circulation to final total jet circulation $\Gamma^*_{v\max}/\Gamma^*_{t\max}$ is presented in Fig. 9. In general, the ratio decreases with increasing stroke ratio due to the appearance of a trailing jet for both nozzles. Even at a small stroke ratio less than the formation number, not all the trailing jet can be absorbed into the vortex ring after the termination of piston motion because the vortex ring actually moves faster with its own self-induced velocity [see a drop in Fig. 8(a) for the green line]. A smaller ratio for case T1 that for than case T2 can be explained by the opposite vorticity of the stopping vortex generated by the termination of piston motion. It is suggested that the stroke ratio should not
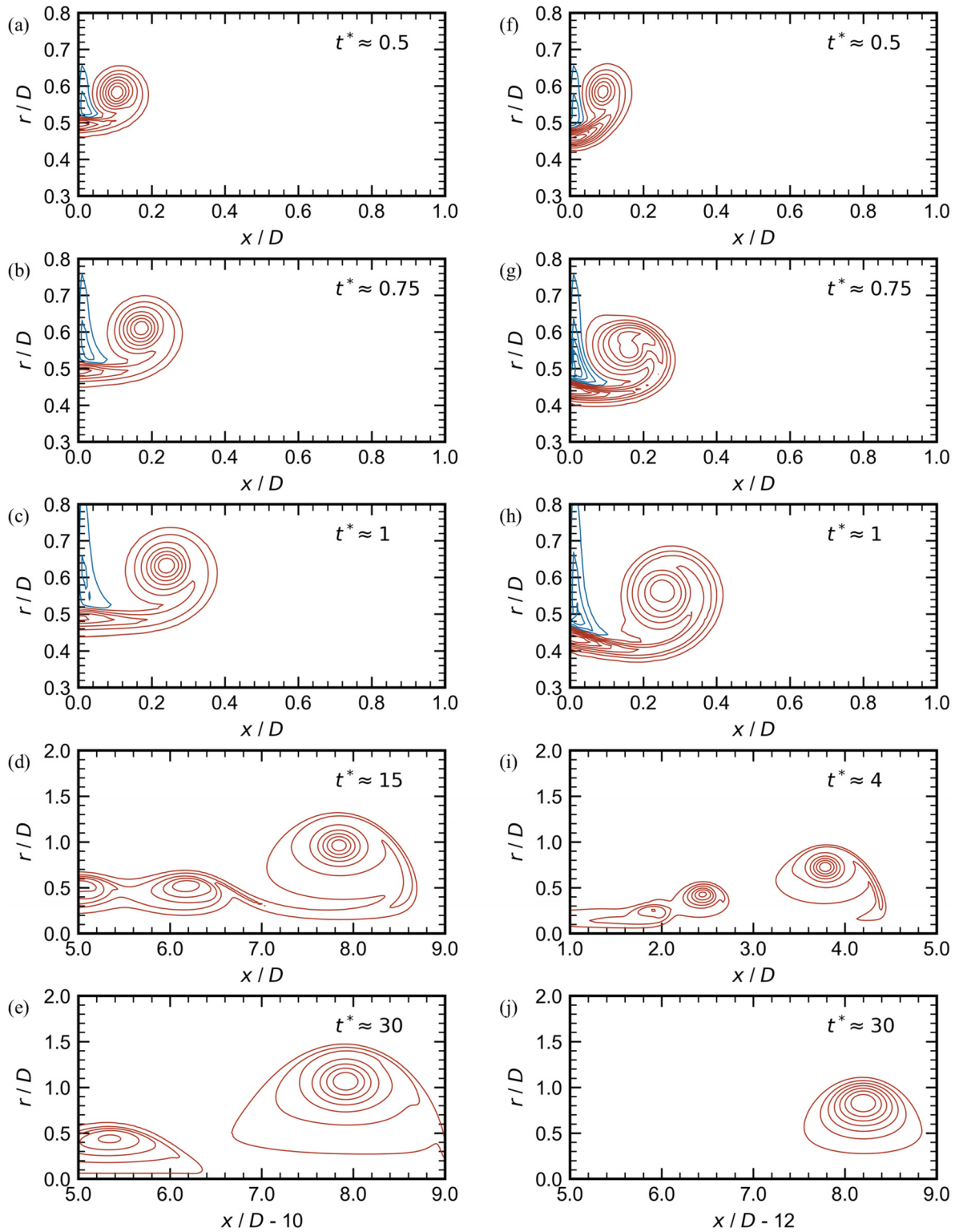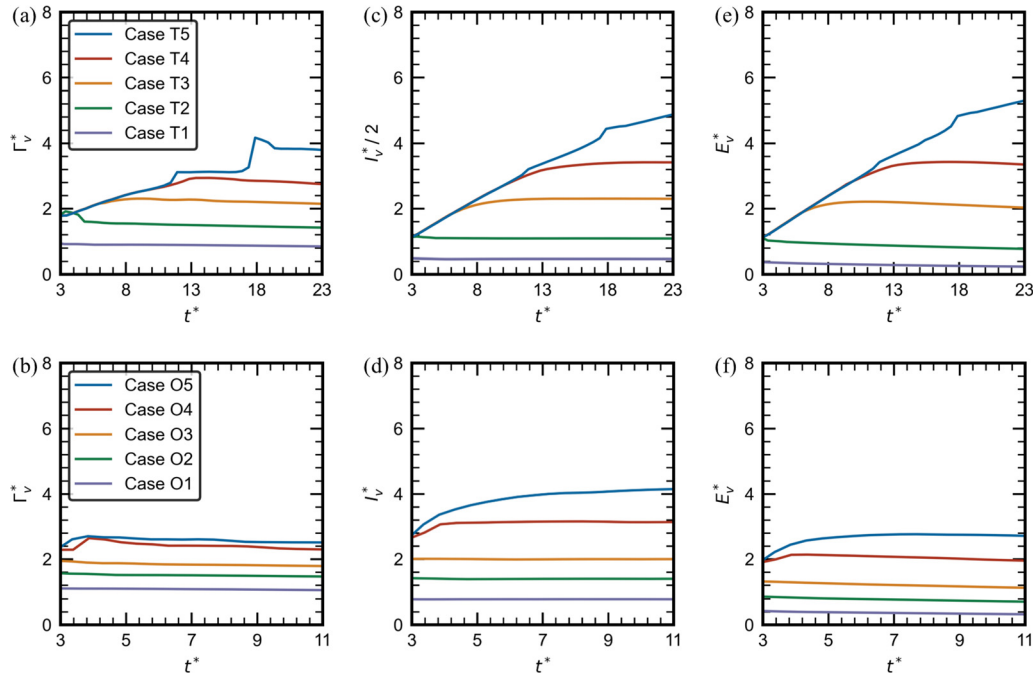
FIG. 6. Vorticity fields normalized by the local maximum for (a)–(e) the tube with stroke ratio 15 and (f)–(j) the orifice with stroke ratio 4. Both positive and negative vorticity fields are with eight levels from absolute 0.05 to 1.
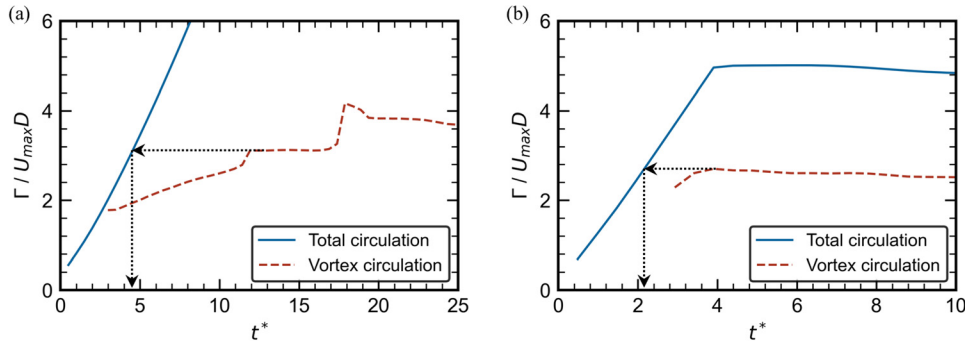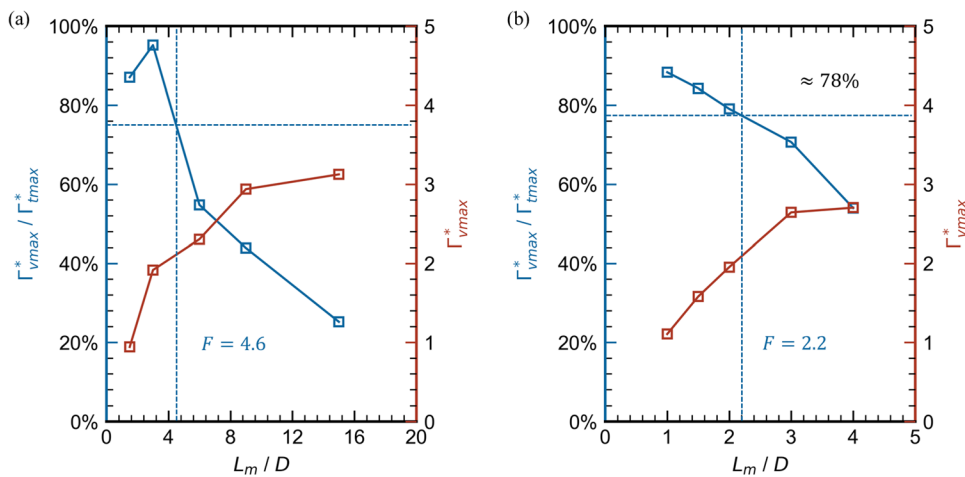
FIG. 7. Normalized circulation of the total jet and the leading vortex ring as a function of time for (a) tube case T5 and (b) orifice case O5.

FIG. 8. Evolution of vortex invariants: (a) and (b) circulation, for (c) and (d) impulse, and (e) and (f) energy. Rows represent tube and orifice cases from top to bottom.

FIG. 9. Circulation ratio of vortex formation and locally maximum vortex circulation vs the stroke ratio for (a) tube and (b) orifice.

be too small if a larger ratio is desired. The significant increase in vortex circulation by vortex pairing only brings a slight increase in the circulation ratio. The growth rates of vortex circulation decline as the stroke ratio increases for both nozzles, implying a limiting vortex growth.

It is surprising to see that the circulation ratio drops simultaneously to about 78% for both parallel starting jets. This happens when the stroke ratios become the same as their formation numbers (blue lines in Fig. 9 for $L_m/D = F$). The critical stroke ratios 4 and 2 suggested by experiments[16,19] for tube and orifice both correspond to about 80% in the circulation ratio. This property could be considered as an alternative criterion for the onset of the pinch-off.[16] With the vortex growth, the high-pressure rear boundary can form a barrier to suppress the upstream delivery of the jet fluid. When the ratio $\Gamma^*_{v\max}/\Gamma^*_{t\max}$ becomes less than 80%, the barrier becomes strong enough to start decreasing the circulation increase to a negligible value. The result suggests that stroke ratios that are larger than the formation number would generate vortex rings with less convection due to a stronger rear vortex boundary [e.g., Fig. 5(d)].

B. Similarity model during the formation stage for tube-generated and orifice-generated starting jets

This section would further discuss the kinematical properties of vortex rings and their relations with dynamical properties. The scaling laws for vortex trajectories at small times ($t^* \leq 1.6$) have been extensively studied for the tube case only.[8,11,12] To provide more details at a larger formation time [$t^* = L(t)/D > 2$], the scaling laws would be investigated for both tube and orifice cases in this section. According to Saffman's inviscid velocity formula,[22,34] the non-dimensional energy can be obtained by vortex trajectories and circulation, i.e.,

$$\sqrt{\pi} E_v^{**} + 3/4 = \frac{\pi U_v D_v}{\Gamma_v} = \frac{\pi U_v^* D_v^*}{\Gamma_v^*}, \qquad (4)$$

where U_v^* and D_v^* are $U_v/U_{\max}$ and D_v/D. The ring translational velocity U_v^* and ring diameter D_v^* are obtained from the ring axial $x_v^* = x_v/D$ and radial $r_v^* = r_v/D$ trajectories.

The scaling laws for the axial trajectory are presented in Fig. 10. Case T3 and case O5 are discussed primarily in this section due to their large stroke ratios. The fitted lines for case T3 and O5 are obtained by the least squares method. At the initial time $0 \leq t^* \leq 1$, the 3/2 power law found by previous experiments[8] can be confirmed in our simulations for both tube and orifice cases. It is noted that the proposed 4/3 law can describe both the small time $t^* < 0.8$ and larger time $0.8 \leq t^* \leq 1$ [Fig. 10(a)]. Moreover, the 4/3 law can predict the axial trajectory over a wide range of time $0 \leq t^* \leq 6$.[11] The fits are therefore divided into two stages $0 \leq t^* \leq 1$ and $1 \leq t^* \leq 6$ for the tube case [e.g., the red and yellow dashed lines in Fig. 10(a)]. Due to the *vena contracta* effect caused by the orifice plate, the accelerated vortex allows a 3/2 power law at $1 \leq t^* \leq 3$ and decreases to a 4/3 power-law acceleration at $3 \leq t^* \leq 6$ [Fig. 10(b)].

Following the previous experiments[8] and established theory,[9,10] the 2/3 law is able to predict the radial trajectory for both tube and orifice at the initial formation time, i.e., $0 \leq t^* \leq 0.5$ [Figs. 11(a) and 11(b)]. However, the increase in the ring radius is perturbed due to the convergent flow ejected from the orifice and the negative vorticity on the outer orifice plate at $t^* > 0.5$. The power for the tube continually decreases to 1/2 at $1 \leq t^* \leq 3$ and 2/5 at $3 \leq t^* \leq 6$ [Fig. 11(a)]. The result suggests a decline in the growth of vortex formation. Although the radial trajectory is perturbed in the orifice case, it basically follows the 2/3 power law at $1 \leq t^* \leq 4$ with a smaller scaling factor than that during the initial formation. After the stop of jet discharge $t^* > 4$, the growth of radial trajectory drops to an even smaller index power of 1/5 for the orifice case [Fig. 11(b)]. As shown in Fig. 11, the trajectory of cases with small stroke ratio (such as cases T1 and O2) would drop due to the influence of wall boundary and stopping vortex with negative vorticity near the nozzle exit. This leads to a deviation from the scaling laws. Even for cases without much influence from stopping vortex (such as cases T2 and O3), the development of ring radius would also deviate from scaling laws and stop temporally. During this process after the termination of jet discharge, the vortex ring redistributes its vorticity and stabilizes itself.
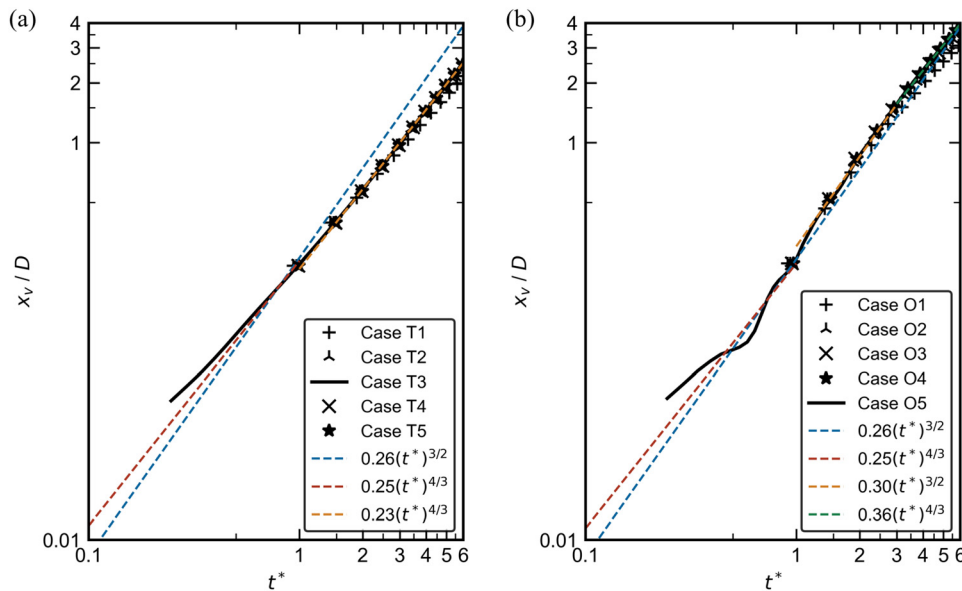

FIG. 10. Evolution of axial trajectory and corresponding power-law fit during the formation stage for (a) tube and (b) orifice.
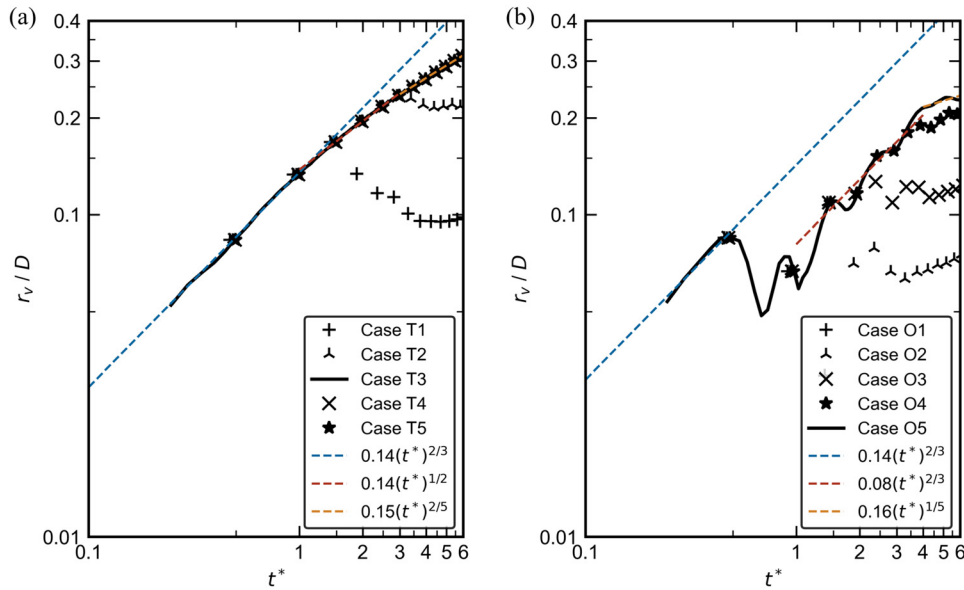
FIG. 11. Evolution of radial trajectory and corresponding power-law fit during the formation stage for (a) tube and (b) orifice.

At the initial formation $0 \leq t^* \leq 1$, the total circulation shedding at the nozzle edge could be regarded as the vortex circulation. The fit proposed in tube experiments[8] can predict our simulation well [blue dashed line in Fig. 12(a)]. Moreover, the 2/3 law is found to be more appropriate for describing initial vortex shedding [Fig. 12(a)]. With the vortex rear boundary, which can only be identified at larger time $t^* \geq 3$, the 2/3 law becomes less agreeable as shown in Fig. 12(a). The growth of vortex circulation allows a 1/3 law at $t^* \geq 3$, which is less than the 2/3 law in the initial formation. This implies a declining growth of vortex due to the growing rear boundary to reject trailing vorticity. For small-stroke-ratio cases T1 and T2, vortex rings stop absorbing circulation and start decreasing due to viscosity diffusion. For the orifice, a linear scaling law can best fit the vortex shedding

[Fig. 12(b)]. The larger power than that for the tube can be attributed to the additional vorticity from the non-parallel starting flow.

Substituting the power-law fits for trajectories and vortex circulation in Saffman's formula [Eq. (4)], the evolution of vortex energy in a non-dimensional form can be obtained. At the initial formation $0 \leq t^* \leq 1$, vortex energy for the tube and orifice can be written as

$$\sqrt{\pi} E_v^{**} + 3/4 = \frac{\pi U_v^* D_v^*}{\Gamma_v^*} = \frac{4\pi a_x (t^*)^{1/3} \times 2 \left[0.5 + a_r (t^*)^{2/3}\right]}{3 a_\Gamma (t^*)^{2/3}}$$

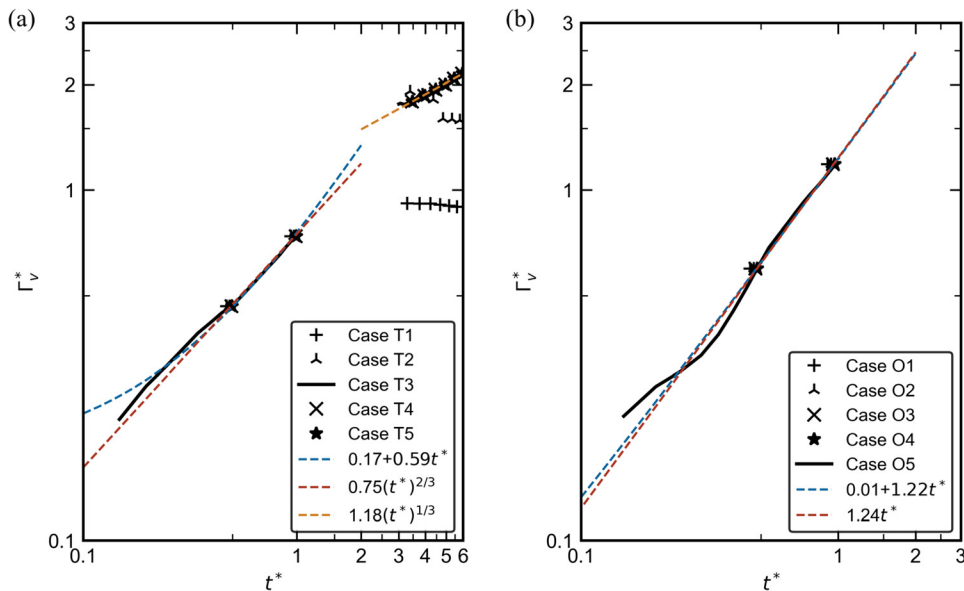$$= \frac{4\pi a_x + 8\pi a_x a_r (t^*)^{2/3}}{3 a_\Gamma (t^*)^{1/3}}, \quad (5)$$

FIG. 12. Evolution of vortex circulation and corresponding power-law fit during the formation stage for (a) tube and (b) orifice.
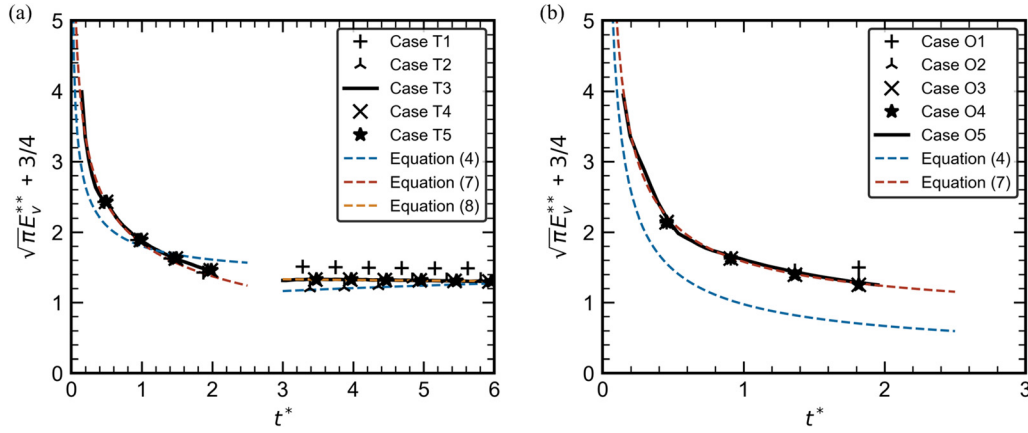
FIG. 13. Evolution of vortex energy and corresponding power-law fit during the formation stage for (a) tube and (b) orifice.

$$\sqrt{\pi}E_v^{**} + 3/4 = \frac{\pi U_v^* D_v^*}{\Gamma_v^*} = \frac{4\pi a_x + 8\pi a_x a_r (t^*)^{2/3}}{3a_\Gamma (t^*)^{2/3}}, \quad (6)$$

where positive constants (i.e., scaling factors) a_x, a_r, and a_Γ can be estimated from fitting power laws for x_v^*, r_v^*, and Γ_v^*. As shown in Figs. 13(a) and 13(b), Saffman's formula (blue dashed line) can predict the decrease in vortex energy. This corresponds to the thickening of vortex core in vortex formation.[29] The predicted trend of the decrease can be attributed to the circulation growth in the denominator. Nevertheless, Eq. (4) cannot predict the energy value accurately. Motivated by the formula coupled with scaling laws, the vortex energy during the initial formation stage can be rewritten for the tube and orifice cases in the form of

$$\sqrt{\pi}E_v^{**} + 3/4 = \frac{a_{ne} + b_{ne}(t^*)^{2/3}}{(t^*)^{1/3}} \quad \text{and} \quad \sqrt{\pi}E_v^{**} + 3/4 = \frac{a_{ne} + b_{ne}(t^*)^{2/3}}{(t^*)^{2/3}}, \quad (7)$$

where constants a_{ne} and b_{ne} (see Table III) are obtained from the fitting procedures. As shown in Figs. 13(a) and 13(b), these semi-empirical forms can accurately describe energy evolution.

Saffman's formula has also been used to predict the energy evolution at larger time $t^* \geq 3$ for the tube case. The error could be insignificant. Considering the expression with scaling laws, the vortex energy can be written as

$$\sqrt{\pi}E_v^{**} + 3/4 = a_{ne} + b_{ne}(t^*)^{2/5}. \quad (8)$$

This above-mentioned expression can fit the energy variation well for the tube case [Fig. 13(a)].

TABLE III. Parameters used to fit the evolution of non-dimensional vortex energy during the formation stage.

Case	Time	a_{ne}	b_{ne}
T3	$0 \leq t^* \leq 1$	2.03	−0.19
T3	$t^* \geq 3$	1.41	−0.05
O3	$0 \leq t^* \leq 1$	0.93	0.69

C. Similarity model during the post-formation stage for tube-generated and orifice-generated starting jets

Following the last section, the scaling laws and prediction of vortex properties during the post-formation stage would be studied in this section. During the post-formation stage, the orifice-based experiments[13] have proposed scaling laws for the laminar vortex rings. They can be written as

$$(R_v^*)^3 \sim t_2^* \quad \text{and} \quad U_v^* \sim (t_2^*)^{-1}. \quad (9)$$

A shift time $t_2^* = t^* - t_0^*$ is defined with the virtual origin time t_0^* determined by a linear fit $(R_v^*)^3 \sim t_2^*$ for each case. When the core radius a is comparable with the ring diameter D_v, the vortex impulse follows the scaling law,[34] i.e.,

$$I_v^* \sim U_v^* (R_v^*)^3. \quad (10)$$

Considering the measurements,[13] the assumption of constant impulse $I_v^* \sim 1$ can thus be achieved. From the asymptotic relation,[34] the vortex impulse can be expressed in terms of the vortex circulation, such as

$$I_v^* = \pi (R_v^*)^2 \Gamma_v^*. \quad (11)$$

As a result, the scaling law for the decay of vortex strength can be written as

$$\Gamma_v^* \sim (t_2^*)^{-2/3}. \quad (12)$$

The -1 power-law decay for translational velocity and the linear increase in $(R_v^*)^3$ have been confirmed in simulations for parallel starting jets.[14] For both tube and orifice, all vortex rings allow the scaling relations (9) and (12) for a wide range of vortex Reynolds numbers $\mathrm{Re}_\Gamma = \Gamma_{vmax}/\nu$ from 2354 to 10418 and $Re_{UD} = (U_v D_v)_{max}/\nu$ from 568 to 1810 (see Fig. 14). It is noted that the vortex Reynold number can be increased by either a larger stroke ratio or the over-pressure effect of the orifice.[23] The ring velocity decay and growth of vortex size (e.g., the ring diameter) are the result of the momentum conservation in an entrainment process. The circulation decay is mainly due to the viscous diffusion of vorticity.
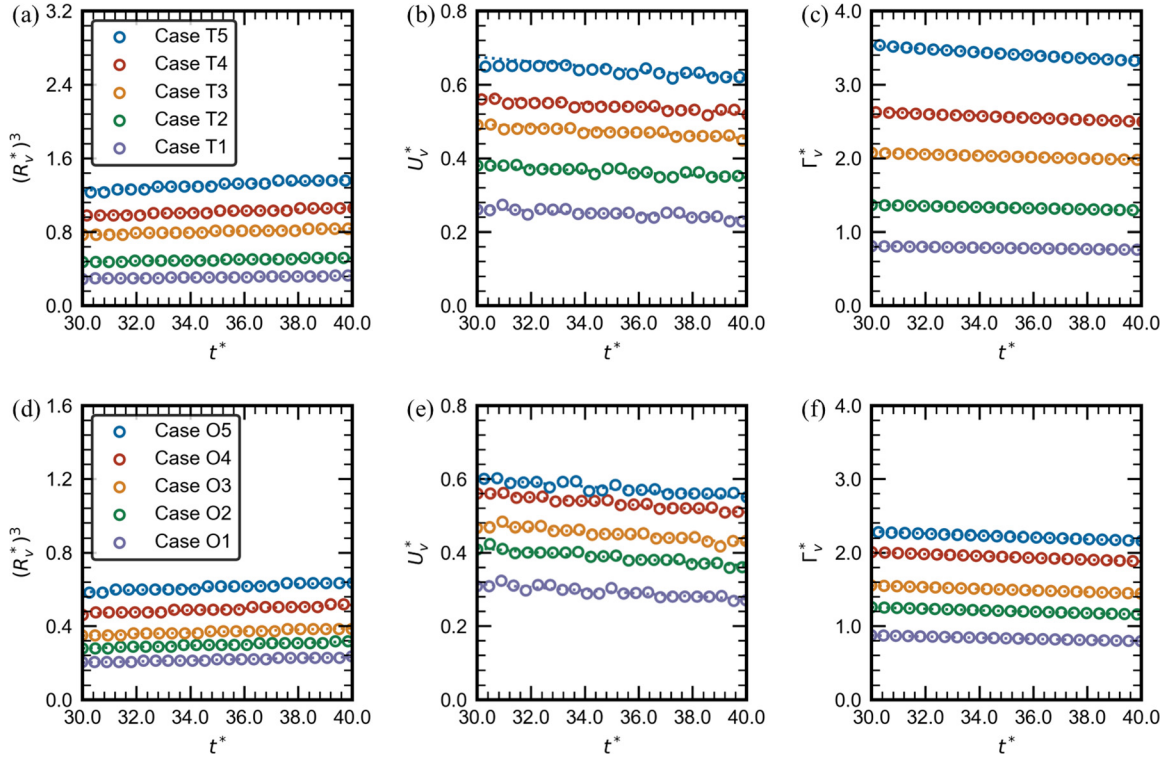
FIG. 14. Evolution of (a) and (d) the magnitude of $(R_v^*)^3$, (b) and (e) translational velocity, and (c) and (f) vortex circulation and corresponding power-law fits during the post-formation stage. Rows from top to bottom represent the tube and orifice.

The invariance of impulse is basically observed for both tube and orifice [found in Figs. 8(c) and 8(d)]. For laminar flows, an obvious vorticity shedding into a wake from the vortex bubble cannot be found. This agrees well with the precondition in the assumption of constant impulse.[13] It is suggested that the invariance of impulse can be satisfied in viscous fluid due to the negligible drag force on vortex rings. It is also independent of vortex Reynolds number and nozzle configurations during the laminar vortex post-formation. Moreover, the results provide strong support for the scaling relation (10) and asymptotic relation in Eq. (11).

During the post-formation stage, the evolutions of non-dimensional energy and circulation are expected to satisfy scaling relations. The average values of non-dimensional energy E_v^{**} are 0.29 and 0.30 for the tube and orifice cases, while the average values of non-dimensional circulation Γ_v^{**} are both 2.04. The limiting values of E_v^{**} and Γ_v^{**} are in agreement with the previous studies.[14,17,19] The evaluation of Eq. (4) is shown in Figs. 15(a) and 15(d) where the average value of the left-hand side of the equation is presented by the black line and the right-hand side obtained by fitted components is presented by color lines. Comparing the average value of colored fitted lines with the black line, errors are at about 6% for both tube and orifice cases. Thus, the invariance of non-dimensional energy can be approximated well by Saffman's formula.

Substituting the scaling relations (9) and (12) in Eq. (4), the vortex energy for both tube and orifice can be written as

$$\sqrt{\pi}E_v^{**} + 3/4 = \frac{\pi U_v^* D_v^*}{\Gamma_v^*} = \frac{\pi a_U (t_2^*)^{-1} \times 2a_R (t_2^*)^{1/3}}{a_\Gamma (t_2^*)^{-2/3}} = \frac{2\pi a_U a_R}{a_\Gamma} \sim 1, \tag{13}$$

where positive constants a_U and a_R (see Table IV) are obtained in fitting power laws for U_v^* and R_v^*. Inserting scaling relations (9) and (12) into Eq. (3), the vortex circulation for both tube and orifice can be written as

$$\Gamma_v^{**} = \frac{\Gamma_v^*}{\left[I_v^* (U_v^*)^2\right]^{1/3}} = \frac{a_\Gamma (t_2^*)^{-2/3}}{\left[a_I a_U^2 (t_2^*)^{-2}\right]^{1/3}} = \frac{a_\Gamma}{a_I^{1/3} a_U^{2/3}} \sim 1, \tag{14}$$

where positive constants a_I (see Table IV) can be obtained from the fitting power laws for I_v^*. The scaling relation (13) is validated in Figs. 15(b) and 15(e), while the scaling relation (14) is validated in Figs. 15(c) and 15(f). The values of E_v^{**} are practically constant, while the values of Γ_v^{**} are in slight oscillation around the averaged value due to the non-circular vortex core. This conclusion agrees well with the previous numerical study.[14] It is suggested that the invariance of dynamical properties ($E_v^{**} \sim \Gamma_v^{**} \sim 1$) is derived on the basis of impulse invariance. As shown in Table IV, the practical constant of E_v^{**} predicted by Eq. (13) can be obtained by the average value 0.33 with deviation ± 0.03. The practical constant of Γ_v^{**} defining by Eq. (14) can be obtained by the average value of 2.04 with deviation within ± 0.04.
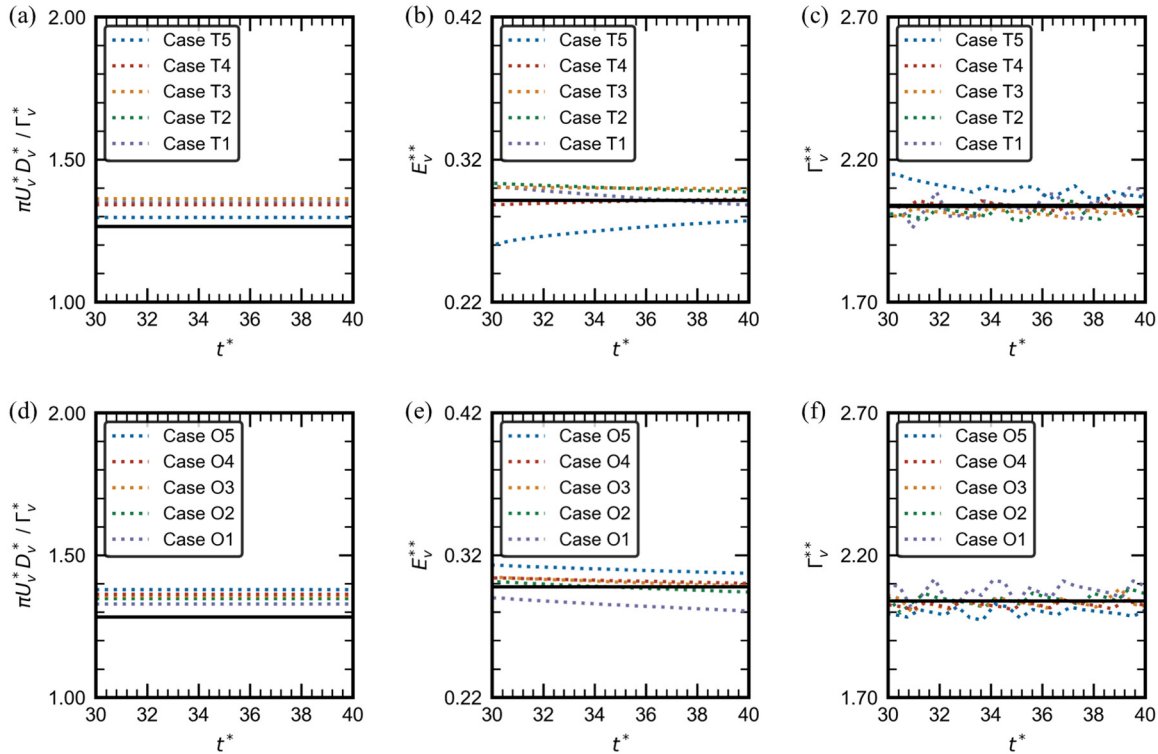
FIG. 15. (a) and (d) Evaluation of Saffman's formula, (b) and (e) the evolution of vortex energy, and (c) and (f) the evolution of vortex circulation during the post-formation stage. Rows from top to bottom represent the tube and orifice. Black lines in the left column indicate the left-hand side of Eq. (4) with non-dimensional energy averaged from simulations. Black lines in the middle and right columns indicate the averaged value of non-dimensional energy and circulation.

TABLE IV. Parameters used to fit the evolution of non-dimensional vortex energy and circulation during the post-formation stage.

Case	t_0^*	a_R	a_U	a_Γ	a_I	E_v^{**}	Γ_v^{**}
T1	−57.82	0.15	23.10	16.06	0.92	0.34	2.04
T2	−77.25	0.16	40.75	30.89	2.15	0.33	2.02
T4	−89.01	0.19	58.63	50.42	4.56	0.36	2.01
T5	−87.21	0.20	66.51	63.18	6.78	0.32	2.03
T6	−76.71	0.23	71.98	79.31	10.68	0.32	2.08
O1	−36.58	0.14	20.95	14.34	0.75	0.30	2.08
O2	−46.91	0.15	31.69	22.71	1.36	0.32	2.05
O3	−56.15	0.16	41.02	30.27	1.96	0.35	2.03
O4	−67.34	0.17	54.59	42.47	3.08	0.35	2.03
O5	−79.35	0.17	65.65	52.32	4.12	0.33	2.01

As shown above, the energy and circulation in the non-dimensional form are related to a constant mean core radius,[29] implying a similarity relation for the size growth of vortex core due to viscous diffusion, such as

$$a^* \sim \left(t_2^*\right)^{1/3}, \tag{15}$$

where the non-dimensional core radius a^* is defined as a/D. To summarize, the scaling laws of vortex evolution (e.g., the non-dimensional

energy E_v^{**}, the non-dimensional circulation Γ_v^{**}, and the diffusivity scale of vortex core a^*) can be derived from Maxworthy's model and Saffman's velocity formula for the tube and orifice cases.

V. CONCLUDING REMARKS

The formation of vortex rings can be used in propulsion systems to enhance propulsive efficiency due to its remarkable mass transport. To further study the kinematic and dynamical properties of laminar vortex rings during the formation stage and the post-formation stage, starting jets generated by tube and orifice nozzles are examined by a series of numerical simulations. By examining the temporal evolutions of vortex properties, the present work focuses on the limiting vortex formation, similarity models in both formation and post-formation stages, and predictions of vortex properties (such as the non-dimensional energy and circulation).

Based on the pressure-based vortex boundary, the growth of vortex invariants is found to be limited by the high-pressure rear barrier. To obtain a vortex ring at maximum circulation, the final stroke ratio must be about twice the formation number for both tube and orifice cases. Based on a ratio $\Gamma_{vmax}^*/\Gamma_{tmax}^*$, an alternative criterion is found to describe the onset of pinch-off (i.e., a critical timescale referred to as the formation number in vortex formation), such as $\Gamma_{vmax}^*/\Gamma_{tmax}^* \approx 80\%$ for $L_m/D = F$. When the stroke ratio is larger than the formation number, the circulation ratio would be lower because more fluids have accumulated in the trailing jet rather than in the leading vortex.

The scaling laws for vortex trajectories found in simulations agree well with experiments and similarity theory at initial time $0 \leq t^* \leq 1$. Some scaling relations are proposed for a larger formation $1 \leq t^* \leq 6$. Based on Saffman's velocity formula together with the proposed scaling laws, the evolution of non-dimensional energy can be predicted accurately for both tube and orifice cases.

During the post-formation stage, the scaling laws measured in experiments are valid for both tube and orifice cases and are independent of the vortex Reynolds number. For the impulse invariance in the decay process, the scaling laws of vortex properties (e.g., E_ν^{**}, Γ_ν^{**}, and a^*) are derived and constant vortex properties (e.g., $E_\nu^{**} \approx 0.3$ and $\Gamma_\nu^{**} \approx 2$) can be accurately predicted by the Saffman's formula. Therefore, the universality for vortex energy and vortex circulation found in experiments[17,19] can be derived from the similarity model for both tube and orifice cases.

When the vortex Reynolds number is low (such as $Re_\Gamma < 1000$), the vortex ring was found to decay with $-3/2$ power law by the Stokes drift as $t \to \infty$.[15] Large viscosity could significantly change the decay power. The effects of viscosity on vortex rings generated by tube or orifice nozzles are still not fully understood. For large Reynolds numbers, the vortex ring becomes unstable and significantly sheds vorticity into its wake.[13] The -1 power law would fail for the vortex velocity. The quantitative properties of such vortex rings have not been fully investigated. Future studies would focus on the effects of Reynolds number and nozzle configuration in starting flows.

AUTHOR DECLARATIONS
Conflict of Interest

The authors have no conflicts to disclose.

Author Contributions

Haojun Zheng: Data curation (lead); Formal analysis (equal); Investigation (lead); Methodology (equal); Validation (lead); Visualization (lead); Writing – original draft (equal); Writing – review & editing (equal). **Lei Gao:** Formal analysis (equal); Methodology (equal); Supervision (equal); Writing – original draft (equal); Writing – review & editing (lead). **Simon C. M. Yu:** Formal analysis (equal); Methodology (equal); Supervision (equal); Writing – original draft (equal); Writing – review & editing (equal).

DATA AVAILABILITY

The data that support the findings of this study are available from the corresponding author upon reasonable request.

REFERENCES

[1] J. O. Dabiri, "Optimal vortex formation as a unifying principle in biological propulsion," Annu. Rev. Fluid Mech. **41**, 17–33 (2009).

[2] C. Cummins, M. Seale, A. Macente, D. Certini, E. Mastropaolo, I. M. Viola, and N. Nakayama, "A separated vortex ring underlies the flight of the dandelion," Nature **562**, 414–418 (2018).

[3] F. Pulvirenti, S. Scollo, C. Ferlito, and F. M. Schwandner, "Dynamics of volcanic vortex rings," Sci. Rep. **13**, 2369 (2023).

[4] L. A. Ruiz, R. W. Whittlesey, and J. O. Dabiri, "Vortex-enhanced propulsion," J. Fluid Mech. **668**, 5–32 (2011).

[5] R. W. Whittlesey and J. O. Dabiri, "Optimal vortex formation in a self-propelled vehicle," J. Fluid Mech. **737**, 78–104 (2013).

[6] K. Shariff and A. Leonard, "Vortex rings," Annu. Rev. Fluid Mech. **24**, 235–279 (1992).

[7] I. Danaila, F. Kaplanski, and S. Sazhin, *Vortex Ring Models*, Mathematical Engineering (Springer, 2021).

[8] N. Didden, "On the formation of vortex rings: Rolling-up and production of circulation," J. Appl. Math. Phys. **30**, 101–116 (1979).

[9] P. G. Saffman, "The number of waves on unstable vortex rings," J. Fluid Mech. **84**, 625–639 (1978).

[10] D. I. Pullin, "Vortex ring formation at tube and orifice openings," Phys. Fluids **22**, 401–403 (1979).

[11] M. Nitsche and R. Krasny, "A numerical study of vortex ring formation at the edge of a circular tube," J. Fluid Mech. **276**, 139–161 (1994).

[12] M. Hettel, F. Wetzel, P. Habisreuther, and H. Bockhorn, "Numerical verification of the similarity laws for the formation of laminar vortex rings," J. Fluid Mech. **590**, 35–60 (2007).

[13] T. Maxworthy, "The structure and stability of vortex rings," J. Fluid Mech. **51**, 15–32 (1972).

[14] I. Danaila and J. Helie, "Numerical simulation of the postformation evolution of a laminar vortex ring," Phys. Fluids **20**, 073602 (2008).

[15] T. T. Lim and T. B. Nickels, "Vortex rings," in *Fluid Vortices*, edited by S. I. Green (Springer, Netherlands, 1995), pp. 95–153.

[16] M. Gharib, E. Rambod, and K. Shariff, "A universal time scale for vortex ring formation," J. Fluid Mech. **360**, 121–140 (1998).

[17] K. Mohseni and M. Gharib, "A model for universal time scale of vortex ring formation," Phys. Fluids **10**, 2436–2438 (1998).

[18] K. Mohseni, H. Ran, and T. Colonius, "Numerical experiments on vortex ring formation," J. Fluid Mech. **430**, 267 (2001).

[19] R. Limbourg and J. Nedić, "Formation of an orifice-generated vortex ring," J. Fluid Mech. **913**, A29 (2021).

[20] J. M. Lawson and J. R. Dawson, "The formation of turbulent vortex rings by synthetic jets," Phys. Fluids **25**, 105113 (2013).

[21] K. Schlueter-Kuck and J. O. Dabiri, "Pressure evolution in the shear layer of forming vortex rings," Phys. Rev. Fluids **1**, 012501 (2016).

[22] M. Baskaran and K. Mulleners, "Lagrangian analysis of bio-inspired vortex ring formation," Flow **2**, E16 (2022).

[23] M. Krieg and K. Mohseni, "Modelling circulation, impulse and kinetic energy of starting jets with non-zero radial velocity," J. Fluid Mech. **719**, 488–526 (2013).

[24] R. Limbourg and J. Nedić, "An extended model for orifice starting jets," Phys. Fluids **33**, 067109 (2021).

[25] M. Rosenfeld, E. Rambod, and M. Gharib, "Circulation and formation number of laminar vortex rings," J. Fluid Mech. **376**, 297–318 (1998).

[26] J. Zhu, G. Zhang, L. Gao, and S. C. M. Yu, "The circulation growth of non-impulsive starting jet," Phys. Fluids **35**, 057102 (2023).

[27] J. Zhu, G. Zhang, L. Gao, and S. C. M. Yu, "Vortex ring formation process in starting jets with uniform background co-and counter-flow," J. Fluid Mech. **968**, A26 (2023).

[28] W. Zhao, S. H. Frankel, and L. G. Mongeau, "Effects of trailing jet instability on vortex ring formation," Phys. Fluids **12**, 589–596 (2000).

[29] J. Norbury, "A family of steady vortex rings," J. Fluid Mech. **57**, 417–431 (1973).

[30] M. Krieg and K. Mohseni, "A new kinematic criterion for vortex ring pinch-off," Phys. Fluids **33**, 037120 (2021).

[31] F. B. Kaplanski and Y. A. Rudi, "A model for the formation of "optimal" vortex rings taking into account viscosity," Phys. Fluids **17**, 087101 (2005).

[32] L. Gao and S. C. M. Yu, "Vortex ring formation in starting forced plumes with negative and positive buoyancy," Phys. Fluids **28**, 113601 (2016).

[33] C. O'Farrell and J. O. Dabiri, "A Lagrangian approach to identifying vortex pinch-off," Chaos **20**, 017513 (2010).

[34] P. G. Saffman, "The velocity of viscous vortex rings," Stud. Appl. Math. **49**, 371–380 (1970).